ELSEVIER

Sensors and Actuators A: Physical (2018) 1–23

SNA_2018_903

Revised Manuscript

Modelling and Experimental Validation of Active and Passive Eddy Current Sensors for Blade Tip Timing

Nidhal Jamia[a,*], Michael I. Friswell[a], Sami El-Borgi[b], Prakash Rajendran[c]

[a] *Swansea University*
College of Engineering, Bay Campus
Fabian Way, Crymlyn Burrows,
Swansea SA1 8EN, UK.

[b] *Texas A&M University at Qatar*
Mechanical Engineering Program,
Engineering Building, P.O. Box 23874,
Education City, Doha, Qatar.

[c] *SASTRA Deemed University*
School of Mechanical Engineering,
Thanjavur - 613 401, Tamil Nadu, India.

Abstract

To monitor the vibration of blades in rotating machinery, the contactless method called Blade Tip Timing (BTT) is widely used. Blade vibration and clearance are important diagnostic features for condition monitoring, including the detection of blade cracks. To perform the BTT technique, optical sensors were widely used by industry due to their high accuracy, but the main drawback of these systems is their low tolerance to the presence of contaminants. To overcome this downside, eddy current sensors are a good alternative for health monitoring applications in gas turbines due to their insensitivity to contaminants and debris. This type of sensor has been used by many researchers, predominantly on the experimental side to investigate BTT systems and there is a lack of modelling to support the measurement system design. This paper fills the gap between experiments and modelling for the particular case of a blade rotating past eddy current sensors. Hence the novelty of this paper is the simulation of the BTT application using detailed quasi-static finite element models of the electro-magnetic field to estimate the outputs from active and passive eddy current sensors. A test rig composed of a bladed disk with 12 blades clamped to a rotating shaft was designed and manufactured in order to validate the proposed models with experimental measurements. Finally, a parametric study is presented to show the effect of the blade tip clearance and the rotational speed on the accuracy of the BTT measurement. This leads to better understanding of the sources of error in the time of arrival of the blades passing the sensor and hence insight into the blade vibration measurement accuracy.

Keywords: Passive eddy current sensor, Active eddy current sensor, Blade tip timing, Electro-magnetic field, Quasi-static finite element model

1. Introduction

In turbomachinery, severe vibratory loads may lead to blade failures and therefore the total failure of the engine. Maintenance of the rotating machine is very important and has a tremendous impact on the life cycle cost of the engine. To obtain the best efficiency, an intelligent assessment is necessary for early damage diagnosis and condition based maintenance activities. Initially, contacting sensors such as strain gauges were used to monitor blade response [1]. This approach required mechanical transducers to be attached to several blades to measure the vibration. The shortcomings of this approach include the time required to install the sensors, the fragility of the sensors in the gas turbine environment, and each blade monitored must have its own sensor. Therefore, many investigators have considered contactless diagnostic systems to assess the blade response in the rotating frame, since it is non-intrusive and is able to measure blade vibration in real time and thus enable the prompt detection of potential damage. One of the most widely used methods is the so-called Blade Tip-Timing method (BTT) using sensors mounted on the casing of a machine. This method analyses the time when a blade tip arrives at the position of the stationary sensors, called the blade Time of Arrival (ToA). The blade vibration causes a variation of the ToA and therefore the BTT measurements can be converted to a vibration response as the vibration displacement, frequency and amplitude. In addition to the ToA, the distance separating the blade tip and the sensor mounted in the engine casing, so called the Blade Tip Clearance (BTC), can provide further information to detect damage.

During the early 1970s, Zablotsky and Korostelev [2, 3] introduced the first non-contact measurement based on their own device called ELURA to measure vibration. Their technique was extended by Heath [4] and Heath and Imregun [5] with an enhanced formulation to generate the blade arrival times using optical laser probes. Different sensor technologies have been used to monitor the blade response and position in turbo-machinery, such as optical, capacitance and eddy-current sensors. A review of the technologies used in vibration blade monitoring was summarized by Von Flotow et al. [6]. The need to distinguish between the effect of cracks and other sources of damage on the blade lengthening measurements has been highlighted. In the last decade, crack detection techniques using non-contact blade vibration measurements has witnessed several developments described by Zielinski and Ziller [7, 8] through various experimental applications. Due to the potential of capacitance probes to provide data for both tip clearance and tip timing, Lawson and Ivey [9, 10] investigated blade vibration measurements collected using these sensors. Kempe et al. [11] considered an optical probe due to its low cost and performance at high temperatures to perform proof-of-principle measurements for a novel tip-clearance measurement technique with high spatial and temporal resolution. Sheard [12] described an improved capacitance probe used for high temperature turbine applications. He explored the probe's reliability at high temperatures using blade tip clearance measurement techniques and

*Corresponding author
Email address: 842543@swansea.ac.uk (Nidhal Jamia)

laboratory experiments. In order to overcome several shortcomings of inductive, capacitive and discharging probes in measuring blade tip timing and clearance in turbines, Garcia et al. [13], García et al. [14] proposed a probe based on a trifurcated bundle of optical fibers mounted on the turbine casing. Based on their approach, the tip clearance and blade tip timing measurements were obtained simultaneously, leading to lower cost and time requirements. More recently, Guo et al. [15] performed a model of the blade tip-timing signal from a fiber bundle sensor. They were able to remove the measurement error caused by the variation of the clearance between the blade and the sensor using a variable gain amplifier to amplify the signals to similar levels.

Many researchers have explored the potential of eddy current sensors (ECS) to monitor the health of an engine without any need for direct access to the blade. ECS are also insensitive to the presence of any type of contaminant (e.g. fluid or high temperature). Both tip timing and tip clearance of each blade could be measured by these sensors in real time and at high resolution. However, some limitations such as case thickness or case material could be a major obstacle in monitoring the system. Garcia-Martin et al. [16] reviewed the state-of-the-art of eddy current testing for crack detection in different electrical conductive materials. In terms of experimental studies investigating the eddy current assessment of rotating systems, Lackner [17] assembled a test rig of three spinning test blades to test the ability of ECS in a simulated gas turbine environment. Compared to strain gauge data extracted from the test rig, he showed that ECS could mitigate the drawbacks of other types of sensors, such as optical or capacitive sensors. A numerical model of an ECS for an in-line assessment of hot wire steel was performed by Rahman and Manklein [18]. They used a different numerical method with the aim to model a nondestructive testing system. Chana and Cardwell [19] measured the arrival times of a rotor blade using ECS in various engine trials to evaluate the ability of these sensors to detect pre-existing damage and to capture dynamic foreign object damage events. They obtained high quality tip timing data using ECS. Similarly, Cardwell et al. [20] used ECS to measure blade tip timing in rotating machinery, and developed an improved ECS system through laboratory tests to measure the blade arrival times. Moreover, Chana et al. [21] evaluated the ability of an ECS and a Reasoner software system to isolate a crack propagated in a cyclic engine and to predict its remaining useful life. More recently, a pulsed eddy current technology to monitor the health of the engine through its casing was developed by Mandache et al. [22] based on blade tip displacement. Using a simple 3-blade assembly, a "through the casing" transmit/receive pulsed eddy current probe was employed to investigate variations in blade tip clearance, inter-blade spacing and blade twist/angle. In addition, Liu and Jiang [23] proposed an improved blade tip timing method, and introduced an ECS to detect the torsional vibrations of the rotor. Haase and Haase [24] used through-the-case ECS to advance tip clearance measurement systems for turbine engines. Using a combination of ECS and optical sensors, Guru et al. [25] instrumented a low pressure turbine stage of a developmental aero engine to monitor blade vibrations during engine tests. In terms of analytical modelling of eddy current fields, Karakoc et al. [26, 27] derived an analytical model of an eddy

current brake (ECB) under time varying magnetic fields, and investigated the effect of the time varying field on the braking torque. To predict small fatigue cracks, Rosell and Person [28] performed an eddy current contactless inspection based on a finite element model and experiments. Wu et al. [29] studied the effect of the motion-induced eddy current (MIEC) on circumferential magnetization in high-speed magnetic flux leakage (MFL) testing. They investigated the effect of rotational speed on the MIEC and circumferential magnetic flux density. They also performed MFL testing experiments for steel pipes to confirm the effect of the MIEC. More recently, Kubín et al. [30] modelled the magnetic interference between ECS and a blade shroud. They proposed a methodology to choose the size of a BTT sensor and where to place this sensor, and they verified their approach through test rig measurements.

The past investigations using eddy current testing in blade tip timing of rotating blades have been predominately experimental. Therefore there is a lack of modelling that can help to understand the error sources in the estimation of the blade time of arrival and hence its effect on the accuracy of the timing measurement, which depends on the blade deformation and clearance between the blade and the sensor. As the requirements from the BTT system becomes more stringent, for example using multiple sensors to extract bending and torsional responses from blades with a complex geometry, the optimization of the measurement system cannot be undertaken experimentally. Further development of BTT systems therefore requires detailed models of both the sensor and the rotating bladed disk. This paper fills the gap between experiments and modelling for the particular case of a blade rotating past eddy current sensors. Hence the novelty of this paper is the simulation of the BTT application using detailed quasi-static finite element models of the electro-magnetic field to estimate the outputs from active and passive eddy current sensors. Hence, for the first time, quasi-static 3-D finite element models of the electro-magnetic field are developed in this paper to simulate the integrated measured output from an Active Eddy Current Sensor (A-ECS) and a Passive Eddy Current Sensor (P-ECS). The blade time of arrival will depend on the amplitude and frequency of vibration and therefore the blade motion can be characterised by the knowledge of such data An integral test rig was designed and manufactured to generate BTT outputs in order to validate the models of the ECS.

This paper is arranged as follows. The basic theory of eddy current sensors in monitoring a moving target, including the governing equations to model a moving target in an electro-magnetic field are described in Section 2. Two numerical models for blade tip timing using P-ECS and A-ECS are described in details in Section 3, where the details of the meshing and boundary conditions are described and simulation results are presented. A description of the test rig design and fabrication, with the validation of models with experimental measurements, are presented in Section 4. Section 5 gives a parametric study and the paper ends with concluding remarks.

2. Basic theory of ECS in sensing a moving target

2.1. Fundamental principle of ECS

In this section the concept of eddy current monitoring a moving target is described. Two types of eddy current sensors exist, namely A-ECS and P-ECS. In the case of a P-ECS, if a conductive target moves through a permanent magnetic field, eddy currents are generated. In contrast, when an alternating magnetic field acts on a conductive target, this case corresponds to an A-ECS. These two types of sensors have been used in BTT applications. In the following, the operating concept of an A-ECS is described [16]. A time-varying magnetic field generated by an alternating current in the coil of the ECS is formed around the coil. If an electrically conducting target is moving past, the primary magnetic field penetrates the moving object causing a variation of the magnetic flux through it. Following Faraday's law of induction, this induces a set of electrical closed loops that flow in planes perpendicular to the magnetic field within the conductive target, and are called eddy currents. The current in a given loop is proportional to the area of the loop, to the rate of change of the magnetic field and to the magnetic flux magnitude. Following Lenz's law, the induced currents in the target create a secondary magnetic field that opposes the primary magnetic field and hence the eddy currents affect the primary magnetic field, as shown in Figure 1. This reaction results in a change in the coil impedance which is captured by the sensor. The A-ECS is considered as a displacement sensor, since the change in the coil impedance is related to the gap between the sensor and the target, and commercial sensors are calibrated so that the sensor output is proportional to the relative displacement.
In the case of a P-ECS, the operation process is almost the same, except that a permanent magnetic field is generated, and the motion of the conductive target through the magnetic field generates eddy currents. The secondary magnetic field generated by these eddy currents is measured by the sensor. The magnetic field needs to vary to generate an output in the sensor coil, and hence a P-ECS essentially measures velocity. Thus a P-ECS is not used as a displacement sensor, but does work well for blade tip timing where the blade is always moving past the sensor. Models of both a P-ECS and an A-ECS are considered in this paper.

2.2. Basic physical background for modelling ECS

In this section, the model of an ECS for a moving target is developed. Describing the material properties, in relation to the electromagnetic fields and the corresponding flux densities, the following constitutive relations are considered:

$$D = \varepsilon E \tag{1}$$

$$B = \mu H \tag{2}$$

where E is the electric field vector, H is the magnetic field strength vector, D is the displacement flux density vector, B is the magnetic flux density vector, ε is the electric permittivity and μ is the magnetic permeability

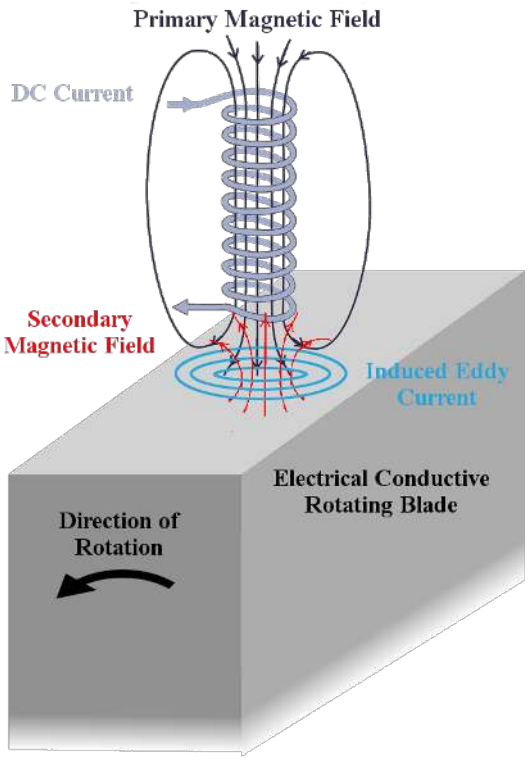

Figure 1: Mechanics of a P-ECS monitoring a moving target

of the medium. For a moving target, the general time-dependent Maxwell's equations (Eqs. (3)–(6)) are used to describe the electro-magnetic field in terms of sources [27, 28]. These equations are written in vector notation and in differential form as:

$$\nabla \times H = J + \frac{\partial D}{\partial t} \tag{3}$$

$$\nabla \times E = -\frac{\partial B}{\partial t} \tag{4}$$

$$\nabla \cdot D = \rho \tag{5}$$

$$\nabla \cdot B = 0 \tag{6}$$

where J is the current density and ρ is the charge density. Satisfying the fourth Maxwell equation (Eq. (6)), a magnetic vector potential A can be defined as,

$$B = \nabla \times A \tag{7}$$

By defining the electric field intensity, and satisfying the second Maxwell's equation (Eq. (4)), the field quantity can be derived from the potential as,

$$E = -\nabla\varphi - \frac{\partial A}{\partial t} \tag{8}$$

where φ is the electric scalar potential. In the particular problem of an eddy current sensor, the electric current generated is composed of two parts and given by

$$J = J_t + J_s \tag{9}$$

where J_t is the current density induced in the electro-conductive target close to the coil sensor and J_s is the current density in the coil region of the sensor generated by the voltage supply in this coil. Following Ohm's law for a moving conductor, along with the presence of the magnetic field, the eddy current generated in the target is defined as

$$J_t = \sigma \left(E + v \times B\right) \tag{10}$$

where v is the velocity of the target and σ is the conductivity of the material of the target.
Since the eddy current problem is a magneto-quasi-static problem [31], the displacement current can be ignored, i.e. $\dfrac{\partial D}{\partial t} \simeq 0$. Therefore, substituting Eqs. (7)–(10) and Eq. (2) into Eq. (3) yields

$$\nabla \times B = \mu\, J + \sigma\, \mu\, \left(E + v \times B\right) \tag{11}$$

By rearranging the terms in Eq. (11) and replacing the electric field and magnetic flux density by their expressions in Eqs. (7)–(8), we obtain, in terms of A and φ, the following magnetic governing equation

$$\nabla \times (\nabla \times A) - \sigma\, \mu \left(-\nabla\varphi - \frac{\partial A}{\partial t} + v \times (\nabla \times A)\right) = \mu\, J_s \tag{12}$$

3. Finite element modelling of ECS monitoring of rotating blades

3.1. Summary of previous models by the authors

Initial investigations by the authors modelled a P-ECS [32], and simulated a rotating bladed disk of simple geometry composed of 4 simplified rectangular blades and surrounded by a casing onto which an eddy current sensor was attached. The aim was to simulate the measurement process used for blade tip timing using ECS. A detailed description of the geometry of the 2-D and 3-D models were described. The simulations gave sensor outputs that corresponded to those measured and reported in the literature. Moreover, the investigation into the sensitivity of the eddy current signal to different model parameters enabled these parameters to be strategically fixed in order to increase damage sensitivity. Furthermore, this modelling approach was utilised to design and optimise the bladed disk test rig presented in the next section.

3.2. Design of the bladed disk

A bladed disk composed of a rotating disk and 12 rectangular twisted removable blades was designed using SolidWorks. Based on the parametric study described in the previous section and performed by Jamia

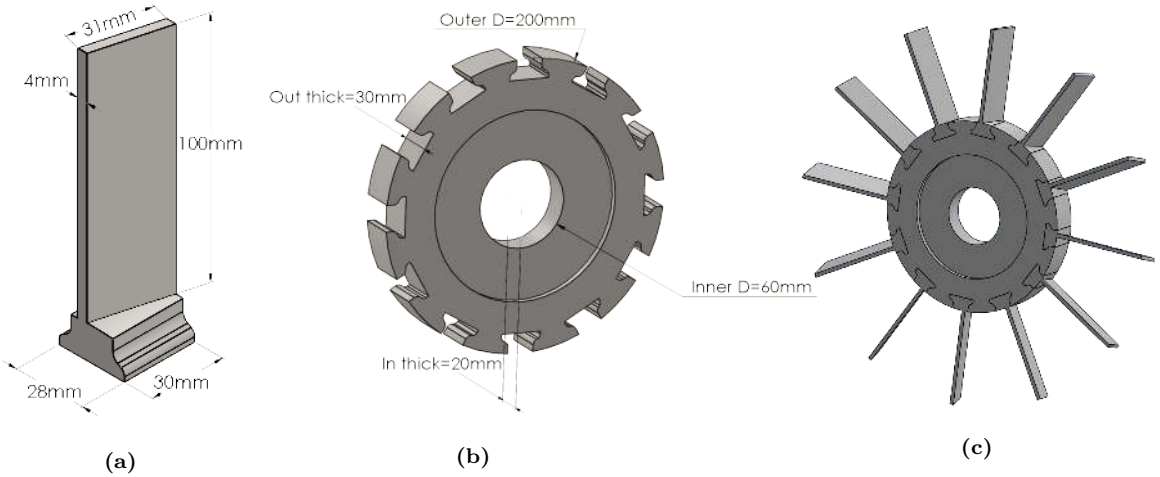

Figure 2: The test rig design (a) Blade (b) Disk (c) Bladed-disk assembly

et al. [32], the initial geometry parameters of the bladed disk were fixed. A rectangular blade with 100 mm length, 31 mm width and 4 mm thickness was designed, as shown in Figure 2a. A detailed modal analysis of the disk was performed using the finite element analysis commercial code ANSYS 16.2., to predict the test response and to guarantee sufficient stiffness of the disk in order to isolate the blade response from the disk response. The outer and inner diameters of the disk were fixed to 200 mm and 60 mm, respectively. The outer thickness of the disk was set at 30 mm and the inner thickness was set at 20 mm, as shown in Figure 2b. Figure 2c shows the assembled bladed disk. Due to the high computational cost of running the models of the bladed disk with 12 blades, a bladed disk with only 2 blades was modelled in the following sections.

3.3. Modelling of P-ECS monitoring a rotating blades

In this section, the modelling of a P-ECS monitoring a rotating bladed disk is described. To achieve this task, a commercial FEA software package, COMSOL Multiphysics® was used [33].

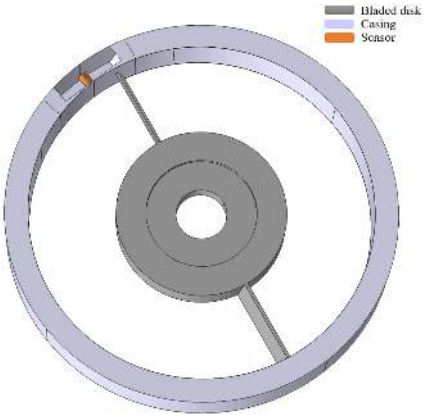

Figure 3: Model geometry of the P-ECS case

The model geometry is first uploaded as a 3D CAD object to the geometry interface of the software. The ECS is represented by a hollow cylindrical with 3 mm inner diameter and 6 mm outer diameter, and is fixed at a distance δ which equals the gap between the blade tip and the sensor. This sensor is mounted to cylindrical casing that surrounds the bladed disk at a distance of $\delta/2$. The material properties of structural steel are assigned to the bladed disk and the casing, and copper material properties are assigned to the core of the sensor. The model geometry is shown in Figure 3 and the material properties are given in Table 1.

Table 1: Material parameters

Parameters	**Air**	**Structural steel**	**Copper**	**Potting material**
Relative permittivity	1	1	1	1
Relative permeability	1	1	1	1
Electrical conductivity	0 [S/m]	4.032e6 [S/m]	5.998e7 [S/m]	0 [S/m]
Young's modulus	-	200e9 [Pa]	110e9 [Pa]	-
Poisson's ratio	-	0.30	0.35	-

The 3-D domain of the model geometry is discretized by cutting the geometry along the air gap into two parts: one containing the static part of the model (the sensor and casing), and the other containing the moving part (i.e. the disk, the blades and the surrounding air), as shown in Figure 4a. The air region between the two parts must be included in the geometry. The highlighted boundary in Figure 4b represents the cut boundary. Tetrahedral elements were used to mesh the different 3D parts of the geometry, while triangular elements were used to mesh the cut boundary. The COMSOL interface uses the moving mesh approach to model the rotation as the finite element method does not naturally support rotations.

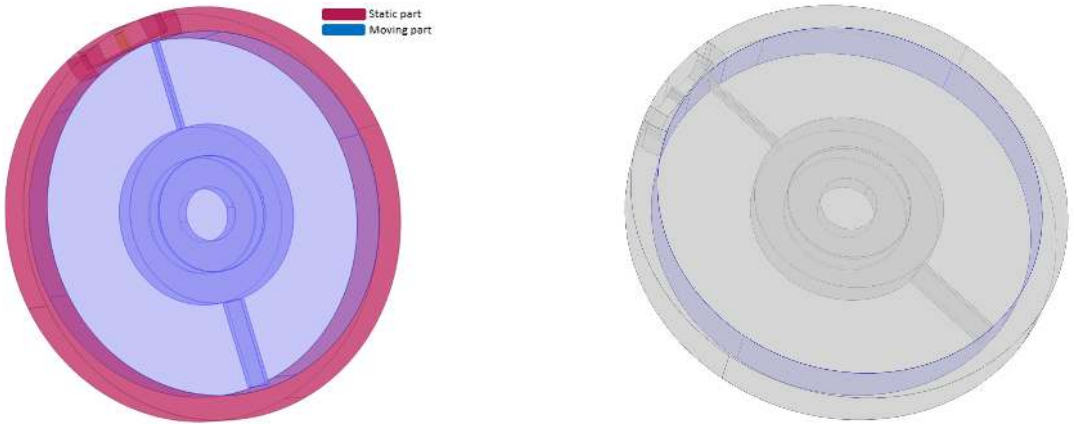

(a) **(b)**

Figure 4: Model geometry of the P-ECS case: (a) Static and moving parts (b) Cut boundary between static and moving parts

The static part remains stationary while the moving part rotates. The two parts are then meshed separately, as shown in Figure 5b by the different positions of the nodes of the mesh on the two sides. Therefore, the meshes slide over each other, remaining always in contact at the cut boundary. Finally, 861810 tetrahedral elements were used for the model, as shown in Figure 5a.

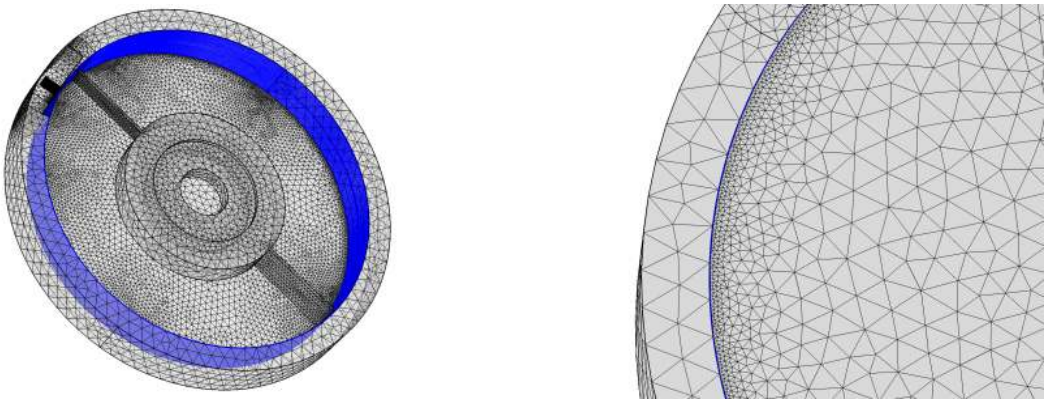

(a) **(b)**

Figure 5: (a) Mesh details of the P-ECS model (b) A close up of the model mesh

The dynamics of the system is defined using the rotating domain interface of COMSOL by applying a rotational velocity to the moving parts. COMSOL enables the moving mesh for the rotating part and guarantees suitable transformations of the electromagnetic field. In time dependent analyses, the quasi-static approximation, which neglects the displacement current density, is applied by the software and therefore all of the currents in the system are induced in the conductive parts or applied externally through the sensor in this case. In order to compute the distribution of the electromagnetic field, COMSOL solves Maxwell's equations using mixed formulations. The vector potential formulation is based on the magnetic vector potential A, which fulfils two of Maxwell's equations (Faraday's law and the magnetic Gauss's law). The second formulation is the scalar potential formulation based on a magnetic scalar potential which is used to define the magnetic field in such away Ampere's law is automatically fulfilled and the magnetic flux conservation law is satisfied. These two formulations are used together by combining the vector potential formulation for conductive domains (e.g. the bladed disk and sensor) and the scalar potential formulation for the free-current domain, such as the surrounding air and air gap. In the case of the sensor, a coil feature from the magnetic field interface in COMSOL was assigned to the hollow cylinder in the model geometry to model the sensor as a conductor subject to an externally applied current or voltage. This feature transforms the applied excitation into local quantities (e.g. electric field and electric current density), and calculated as lumped parameters. The different coil parameters are given in Table 2. The hollow cylinder assigned as a sensor in the model geometry is composed of hollow part representing the core of the sensor with inner diameter D_{inn} and a second cylinder concentric with the first one with an outer diameter D_{out}. These

two dimensions are given in Table 2. The second cylinder contains a multiple tiny wires wound together around a common axis, arranged as a circular coil and placed in a potting material geometry. This wires form a closed circular loop that models the direction of the current flow. The coil wire conductivity, the coil wire cross section area, the coil length and the number of turns given in Table 2 are used to calculate the resistance of the coil as,

$$R_{coil} = \int_A \frac{N_{turn}\, L_{coil}}{\sigma_{coil}\, a_{coil}\, A} \tag{13}$$

Where A is the total cross-sectional area of the coil domain. The coil applies an external current density in the direction of the wires defined as

$$J_e = \frac{N_{turn}\,(V_{coil} + V_{ind})}{R_{coil}\, A} \tag{14}$$

Where V_{ind} is the induced voltage calculated by integrating the electric field along the coil and R_{coil} is the total coil's resistance. In this paper the value of V_{coil} was chosen as a small value due to convergence purposes since increasing this value will results on an important increase of computational cost.

Table 2: Coil parameters

Coil parameters	**Value**	**Unit**	**Name**
Coil excitation	1e-6	V	V_{coil}
Number of turns	500	turn	N_{turn}
Coil wire conductivity	6e7	S/m	σ_{coil}
Coil wire cross-section area	1e-6	m^2	a_{coil}
Coil length	10	mm	L_{coil}
Inner diameter	3	mm	D_{inn}
Outer diameter	5	mm	D_{out}
Coil excited frequency	100	kHz	f_0

In addition, due to convergence issues of the model, the current value in the coil is ramped from a low value using a smoothed step function. Regarding the boundary conditions, the tangential components of the magnetic potential is set to zero at the external boundary due to the magnetic vector potential; on external boundaries with a magnetic scalar potential, the normal component of the magnetic flux density is set to zero. In addition, an identity pair is created connecting the static and moving part which enforces the continuity of the magnetic scalar potential in the global coordinate system.

A time-dependent analysis for an interval of 1.7 s at a rotational speed of 100 rev/min was performed for the P-ECS model. Figure 6a shows the surface plot of the magnetic flux density at the instant when one of the blades passes the sensor. The current density induced throughout the bladed disk is also shown by

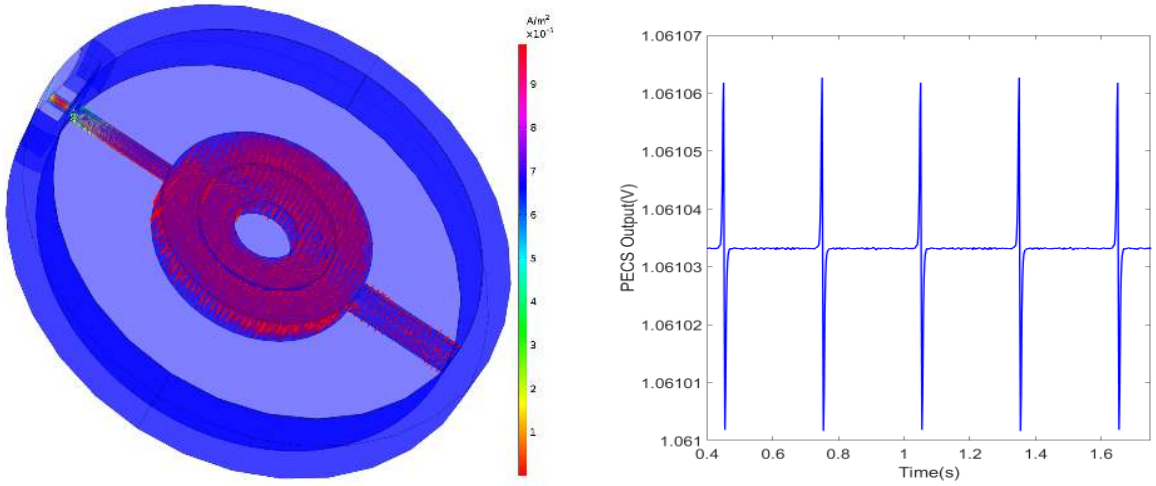

(a) **(b)**

Figure 6: (a) Magnetic flux density (surface) and current density (arrows) for the P-ECS model when a single blade passes the sensor (b) The P-ECS output when several blades pass the sensor

arrows. We can notice a variation in the induced current density at the blade tip. This variation is due to the interference between the primary magnetic field generated by the ECS and the secondary magnetic field generated by the moving blade past the sensor. This agrees with the concept of the P-ECS described in Section 2. Figure 6b shows the corresponding coil voltage captured by the P-ECS when blades pass by. A signal peak is obtained every time a conducting blade enters the field of the sensor which alters the magnetic field through the induced eddy currents in the blades. This describes clearly the behavior of the signal output of the P-ECS; based on a reference voltage which will correspond to a known position on the blade, the time of blade passing can be determined. This gives information about the time of arrival of the blade at the sensor probe. In addition, the shape of a single peak corresponding to the P-ECS case, gives information to determine when the blade is positioned at the middle of the sensor, which gives more detail about the exact blade position.

3.4. Modelling of an A-ECS monitoring rotating blades

This model is based on measuring the change in the coil impedance which is related to the gap between the sensor and the target, and hence the sensor output gives the relative displacement. Therefore, compared to the P-ECS model, the continuous rotation approach is replaced with a series of blade positions using a sweep of the geometry parameter defined as

$$rot\_angle = t\_para * \Omega * 2\,\pi \quad \text{(rad)} \tag{15}$$

where Ω is the rotational speed of the bladed disk, t_para is the parametric time and the blade will rotate with an angle equal to rot_angle with respect to this time. Then, the model is solved as a series of frequency

domain studies whilst rotating the blades in the geometry via a parametric sweep. A frequency domain study defines that an alternative current is used for the coil excitation oscillating at a parameter f_0. This excitation has been set to be 1000 times the rotational speed, to ensure that the quasi-static approximation is valid. A slightly simpler model geometry shown in Figure 7a is used in the case of the A-ECS model.

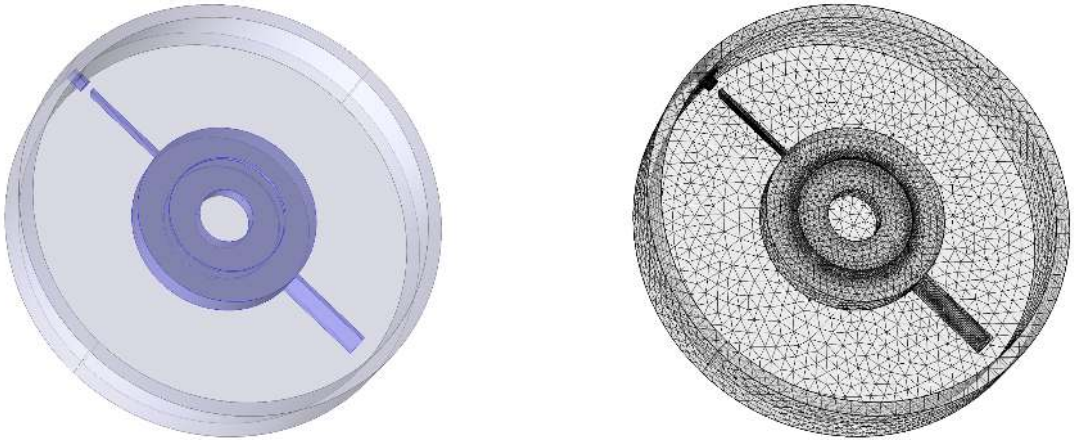

(a) **(b)**

Figure 7: (a) Model geometry of the A-ECS case (b) Mesh details of the A-ECS model

Due to the absence of rotation, the model is solved using the vector potential formulation in all domains. Similarly to the P-ECS model, the coil feature of COMSOL is assigned to the cylinder in the geometry model and the lumped parameter of interest, which is impedance in this case, is calculated. For the meshing of this model, a very fine mesh is used for the blades and the coil; the mesh in the blades has been heavily refined to resolve the currents well. Then, 468634 tetrahedral elements were used for the model, as shown in Figure 7b. Regarding the modelling of the sensor, unlike the P-ECS case, the coil was composed of 100 turns carrying a sinusoidal varying current of 1 A/turn. The magnetic field and the eddy currents induced in the conductor blade is computed for coil currents of frequency f_0 given in Table 2. In a frequency domain study, the impedance variable Z_{coil} is computed as

$$Z_{coil} = \frac{V_{coil}}{I_{coil}} \tag{16}$$

and is proportional to the variation of the magnetic flux due to the interaction between the external magnetic field applied by the sensor and the induced magnetic field by the rotating blade. The values for the coil wire conductivity and cross section area described in Table 2 were used in this model. Finally, the boundary conditions were fixed by the COMSOL interface, considering the tangential components of the magnetic potential is set to zero at the external boundary with magnetic vector potential. The A-ECS model is solved for a full period of rotation of the bladed disk, $T_0 = {}^{2\pi}/_{\Omega}$, for 1000 time steps within that time interval.

Figure 8a shows the surface plot of the magnetic flux density at the instant when one of the blades passes

by the sensor. The current density induced through the bladed disk is also shown by arrows. The eddy currents in the blades induced by the coil result in a variation of the current resistance of the coil. This variation of the coil's impedance causes an electrical signal which is measured by the sensor and calibrated in order to be proportional to the distance between the blade tip and the sensor coil. This signal is shown in Figure 8b. The zero-to-peak amplitude of the signal is determined by the gap; any variation of the gap between the sensor and the blade tip will lead to a variation of the amplitude of the signal.

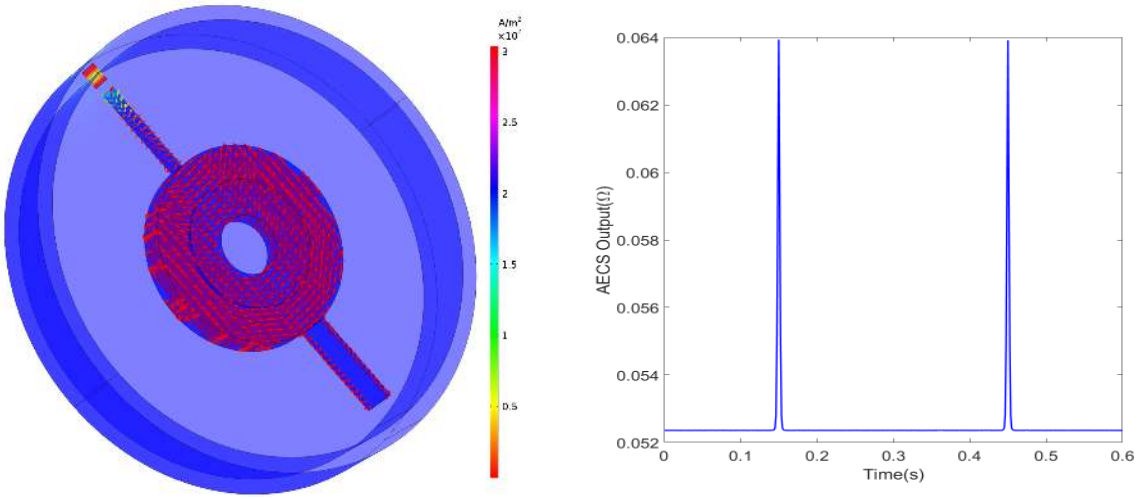

(a) **(b)**

Figure 8: (a) Magnetic flux density (surface) and current density (arrows) for the A-ECS model when a single blade passes the sensor (b) A-ECS output when several blades pass the sensor

4. Experimental program and validation

In this section, the models described above will be validated with measurements collected from a test rig designed and manufactured in the workshop at Swansea University.

4.1. Design and fabrication of test rig

In order to demonstrate the reliability of the models described in this paper, a test rig was designed and manufactured in order to replicate a BTT application and generate BTT measurements using commercial A-ECS and P-ECS and therefore validate the models. Based on a brief review of the literature of the existing test rigs built for monitoring the structural health of a machine [34–38], a test rig was designed that was composed of a bladed disk with 12 blades surrounded by a cylindrical casing. The bladed disk is clamped to the end of a rotating shaft supported by two bearings. In order to avoid any vibration caused by the flexibility of the shaft, a Finite Element Analysis of the shaft was undertaken using ANSYS to ensure that the shaft is effectively rigid. The first natural frequency of the shaft was around 1.2 kHz which is much

higher than the blade first natural frequency, which is around 300 Hz. To provide support for the rotating shaft, two split Plummer block housings are used with compatible ball bearings fitted in the housings. The design of the full test rig is shown in Figure 9. The test rig was fabricated in the machine shop at Swansea

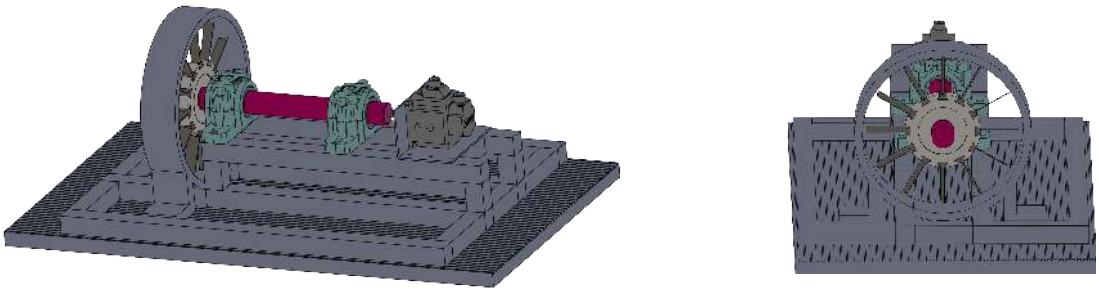

(a) **(b)**

Figure 9: Test rig design: (a) Overall view (b) Side view

University using an EDM machine which uses a very thin wire to accurately cut the blade and disk geometry and decrease the uncertainties that could be introduced through the contact regions. For safety, an acrylic casing was used to cover the entire test rig during operation. The manufactured parts of the test rig are shown in Figure 10.

(a) **(b)**

Figure 10: (a) Manufactured blade (b) Manufactured disk

4.2. Experimental setup and validation

In this section, a description of the experimental setup and the validation of the models with the experimental measurements is presented. In order to replicate the BTT application, the shaft is driven by a Schneider Electric servo drive system composed of a BCH servo motor and an LXM28 (AC servo drive). Two commercial sensors, Active and Passive ECS, were mounted on the casing around the bladed disk through holes, as shown in Figure 11. The sensors were connected to a 4-channel Data Acquisition system (DAQ) in order to measure the sensor outputs. As mentioned earlier, regarding the high computational requirements of the 3-D models of the P-ECS and A-ECS, the simulated model was composed of a disk with two blades,

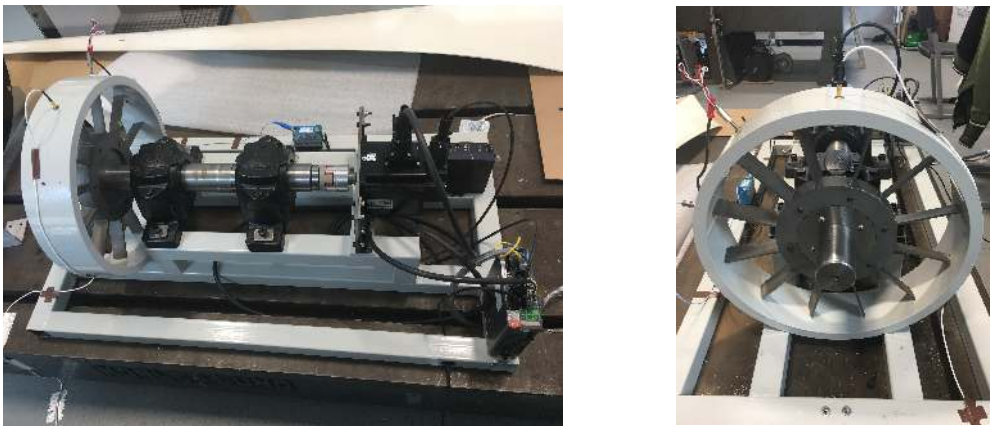

(a) **(b)**

Figure 11: (a) Test rig setup (b) Mounting of the sensors on the casing

which was exported to COMSOL. Therefore, only two blades were installed on the bladed disk to be used to validate the numerical models; retaining blades on opposite sides of the disk ensured that the bladed disk was balanced.

The rotational speed was set to 100 rpm and the clearance between the blade tips and the sensor was 3 mm. The BTT measurements were collected from the A-ECS and P-ECS for a period of 1.28 s at a sampling rate of 13 kHz. Regarding the simulation, the physics based model was updated to predict the same behavior as the commercial sensor by estimating the coil properties such as the number of turns and the coil wire cross section area to give the measured peak sensor output. The comparison of measured output of the P-ECS and the A-ECS, and the numerical results from the models described above are shown in Figure 12 and 13, respectively. These figures show a good agreement between the simulated and measured BTT data for the P-ECS and the A-ECS.

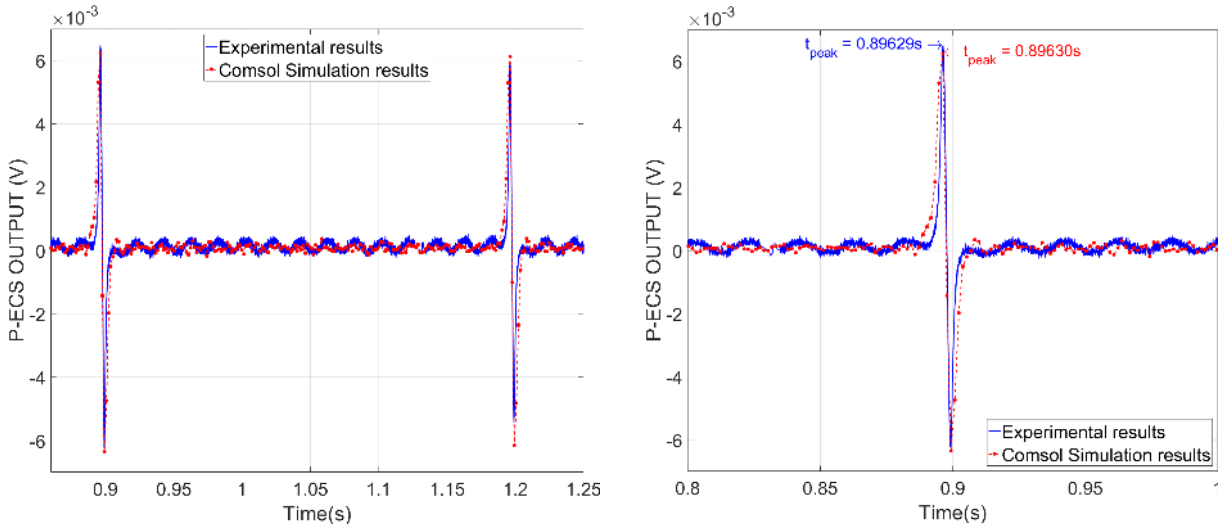

(a) **(b)**

Figure 12: (a) Comparison of experimental measurements with the numerical results from the P-ECS model (b) A locally enlarged graph of Fig. 12a

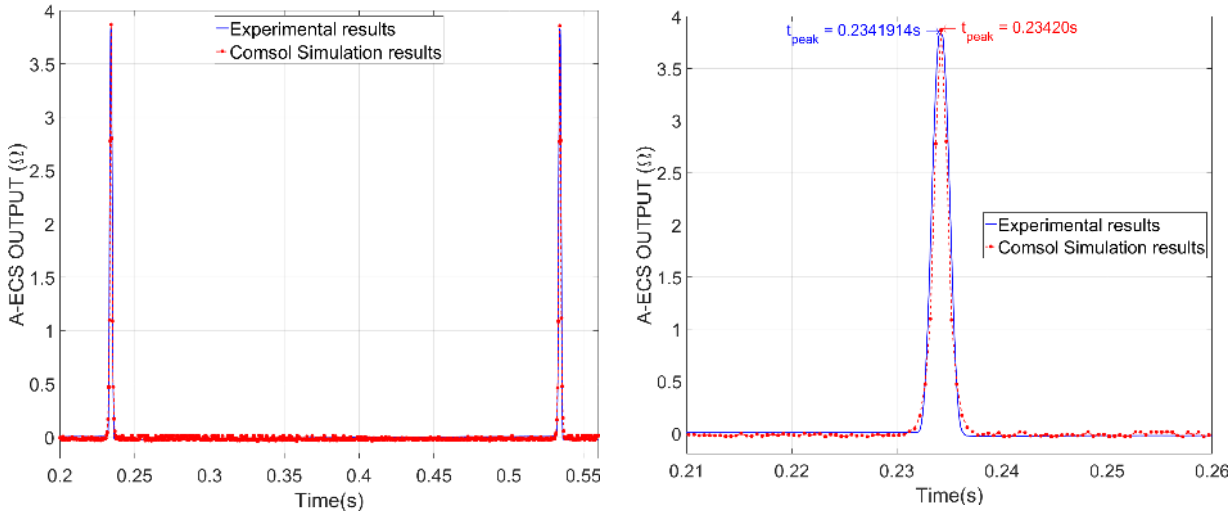

(a) **(b)**

Figure 13: (a) Comparison of experimental measurements with the numerical results from the A-ECS model (b) A locally enlarged graph of Fig. 13a

The accuracy of the ToA measurements is a key parameter for the BTT method. The ToA depends strongly on the threshold picked from the output signal sensors. The sample rate is a key driver for the accuracy of measurements in addition to the level of noise. A high level of noise might lead to errors in picking the accurate threshold corresponding to the ToA of the blade. Depending on the level of noise some techniques can be used to reduce the level of noise, such as cross-correlation or curve fitting methods. Regarding the

simulated measurements, the sample rate can be chosen and then the variation of the noise will be dependent on the mesh element size.

5. Parametric study

In this section, the effect of the variation of the gap (i.e. the distance separating the blade tip and the surface of the sensor during the rotation of the bladed disk) and the bladed disk rotational speed on the output of the A-ECS and P-ECS model was investigated. For the P-ECS model, Figures 14 and 15 show the effect of the gap on the output signal for a range of low and high gaps, respectively. In Figure 14, the amplitude of the signal decreases slightly when the gap increases from 1mm to 3mm in 1mm increments. This agrees with the fact that the maximum speed of the blade is always equal to the tip speed of the blade when it passes the sensor and when the blade aligns with the sensor axis. Therefore, the gap between the sensor tip and the blade tip will not have an important effect on the relative speed for the P-ECS. However, in Figure 15, the variation of the signal output is clearly more significant when the gap increases from 3mm to 9mm. These results show that the P-ECS is relatively insensitive to small distance variations, and it performs well for a higher range of gaps and still can detect the passing of the blade at a large gap (around 10mm).

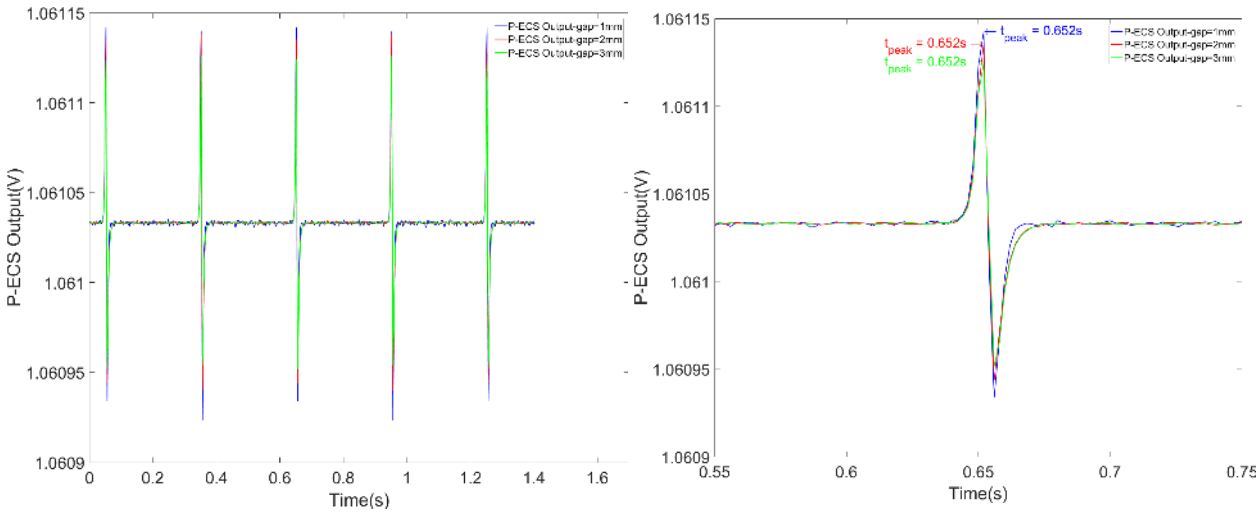

(a) **(b)**

Figure 14: (a) The P-ECS model output for small gaps (b) A locally enlarged graph of Fig. 14a

For the A-ECS model, Figures 16 and 17 show the effect of the gap on the output signal for the gap varying from 1mm to 5mm. Figure 16 shows that the amplitude of the output signal decreases dramatically when the gap increases from 1mm to 3mm. This shows the high sensitivity of the A-ECS to small distance variations, which highlights that this type of sensor is considered as a displacement sensor. As shown in Figure 17,

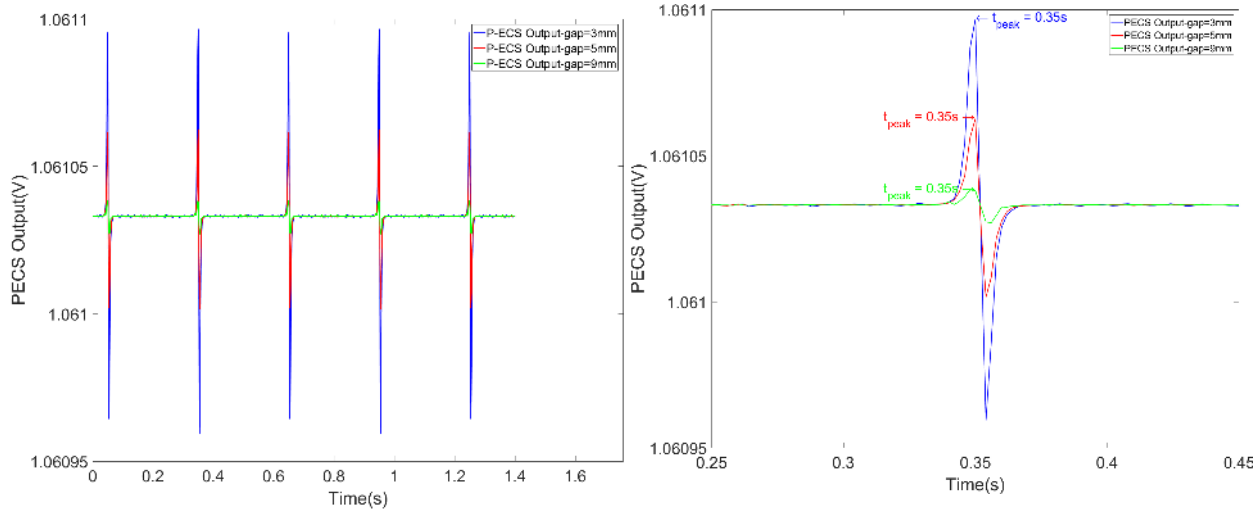

(a) **(b)**

Figure 15: (a) The P-ECS model output for large gaps (b) A locally enlarged graph of Fig. 15a

the output signal becomes very noisy when the gap value is greater than 3 mm and therefore the A-ECS starts to lose its performance in monitoring the rotating blade for larger gaps. In practical applications the effectiveness of the P-ECS for large gaps will be very beneficial.

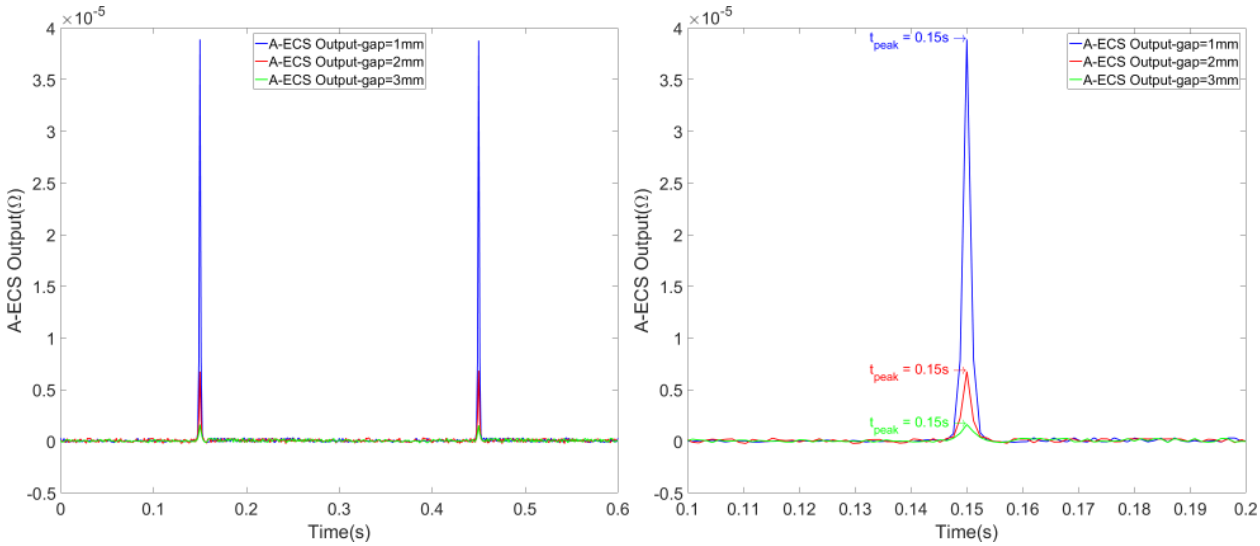

(a) **(b)**

Figure 16: (a) The A-ECS model output for different gaps (b) A locally enlarged graph of Fig. 16a

Finally, Figure 18 shows the effect of the rotational speed of the bladed disk on the P-ECS and A-ECS outputs. Due to the difficulty in analysing the raw results in this case, the signal outputs have been shifted

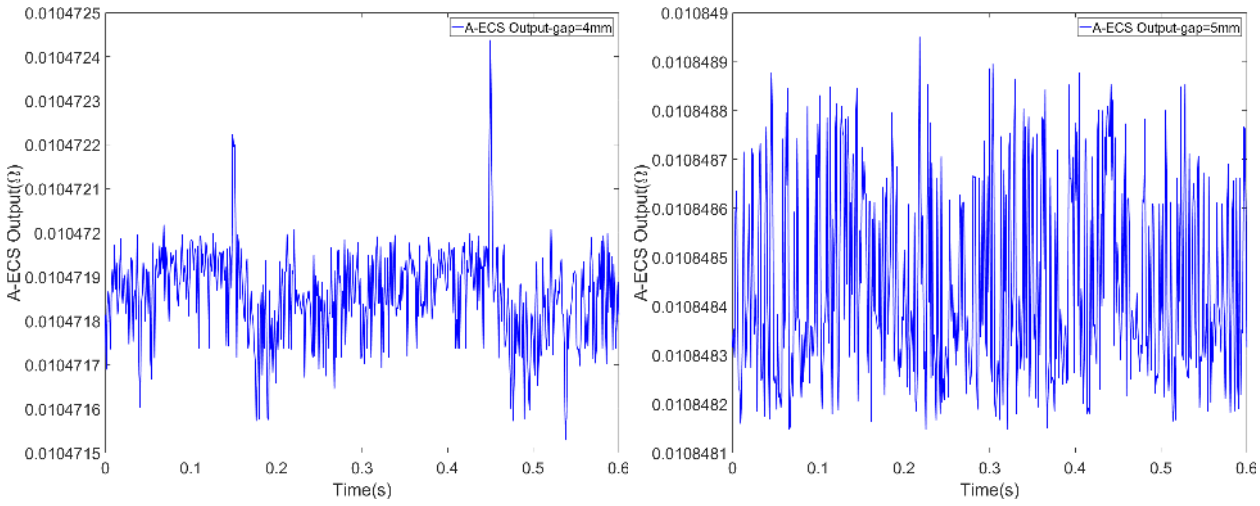

(a) **(b)**

Figure 17: A-ECS signal output with time corresponding to (a) Gap=4mm (b) Gap=5mm

to a common point so that the blade passes the sensor at the same time.

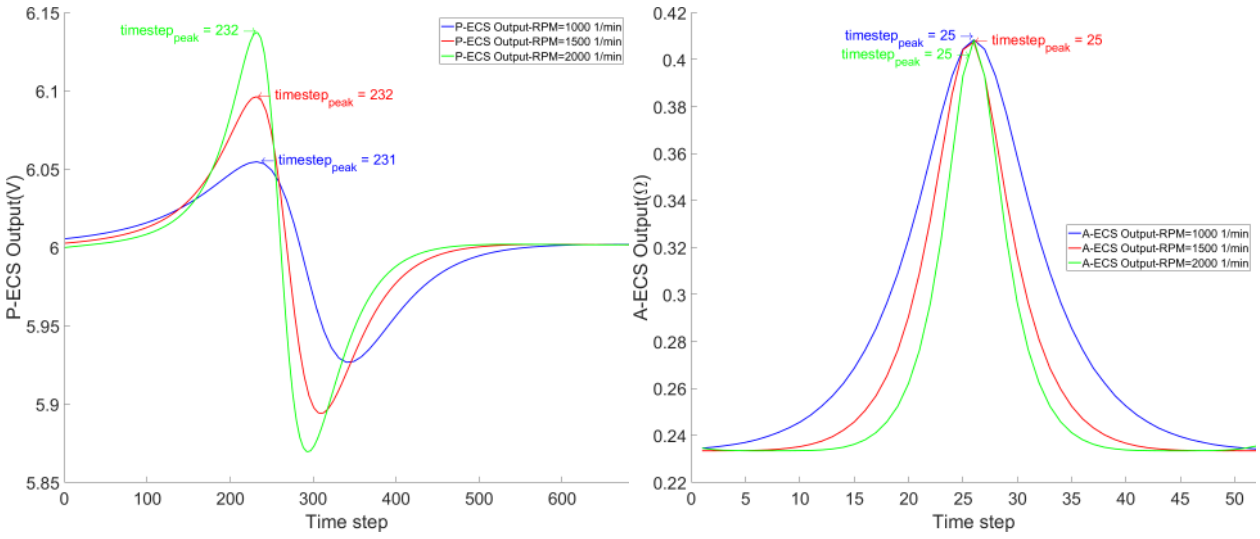

(a) **(b)**

Figure 18: The sensor output with time for different rotational speeds (curves shifted to a common point) (a) P-ECS model (b) A-ECS model

For the P-ECS case, Figure 18a shows an increase of the signal amplitude with increasing rotational speed. This shows the sensitivity of this type of sensor with the speed variation and which highlights that the P-ECS is considered as a speed sensor and not as a displacement sensor; the magnetic field in the P-ECS is obtained from a permanent magnetic and hence the change in magnetic field flux is due to the velocity of

the blade. However, Figure 18b shows the insensitivity of the A-ECS model output with the speed variation which demonstrates that the A-ECS is behaving as a displacement sensor, This parametric study leads to the conclusion that the P-ECS could be more efficient for the BTT measurement due to its high sensitivity to the velocity of the blade.

6. Conclusion

This paper has simulated a rotating bladed disk monitored by passive and active eddy current sensors mounted on a casing surrounding the bladed disk. The aim was to simulate the measurement process used for blade tip timing using eddy current sensors. Eddy current sensors have been considered in this paper due to their robustness in harsh environments. The governing equations modelling the electro-magnetic field of a moving target have been described for a quasi-static problem. A detailed description of the 3-D models for a P-ECS model and an A-ECS model were presented, together with the rotating mesh details, and the physics of the electro-magnetic fields. A test rig was designed and manufactured in order to generate BTT measurements for P-ECS and A-ECS. These measurements were used to validate the numerical models. Finally, a parametric study was performed to study the effect of the gap and rotational speed on the outputs from the sensors. The results showed that the A-ECS output is more sensitive to the gap between blade tip and sensor than the P-ECS, while this latter is more sensitive to the blade velocity than the A-ECS. This sensitivity can help to estimate more accurately the time of arrival of the blade by taking in consideration these effects. In addition it was concluded that the P-ECS can be more accurate for BTT measurements. The proposed modelling approach can be utilised to design more complex BTT applications with multiple sensors and complex geometries. Finally, a BTT study to identify damage in vibrating blades while they are rotating will be the subject of future research.

Acknowledgment

The authors gratefully acknowledge the support of the Qatar National Research Fund through grant number NPRP 7-1153-2-432.

Declaration of interest: None

Bibliography

[1] C. Fangman, V. Zastrow, J. Bobeck, High-speed-turbocharger blade-vibration mesurement, Experimental Mechanics 7 (1) (1967) 19A–21A.

[2] I. Zablotskii, Y. A. Korostelev, L. Sviblov, Contactless measuring of vibrations in the rotor blades of turbines, Tech. Rep., Foreign technology div Wright-Patterson AFB OH, 1974.

[3] I. Y. Zablotskiy, Y. A. Korostelev, Measurement of resonance vibrations of turbine blades with the ELURA device, Tech. Rep., Foreign Technology Div Wright-Patterson AFB OH, 1978.

[4] S. Heath, A study of tip-timing measurement techniques for the determination of bladed-disk vibration characteristics, Ph.D. thesis, University of London, 1997.

[5] S. Heath, M. Imregun, An improved single-parameter tip-timing method for turbomachinery blade vibration measurements using optical laser probes, International journal of mechanical sciences 38 (10) (1996) 1047–1058.

[6] A. Von Flotow, M. Mercadal, P. Tappert, Health monitoring and prognostics of blades and disks with blade tip sensors, in: Aerospace Conference Proceedings, 2000 IEEE, vol. 6, IEEE, 433–440, 2000.

[7] M. Zielinski, G. Ziller, Noncontact vibration measurements on compressor rotor blades, Measurement Science and Technology 11 (7) (2000) 847.

[8] M. Zielinski, G. Ziller, Noncontact blade vibration measurement system for aero engine application, in: 17th International Symposium on Airbreathing Engines, vol. 11, 244, 2005.

[9] C. Lawson, P. Ivey, The use of commercially available capacitance tip-clearance probes for tip-timing of aero-engine compressor blades, in: 38th AIAA/ASME/SAE/ASEE Joint Propulsion Conference & Exhibit, 3730, 2002.

[10] C. P. Lawson, P. C. Ivey, Tubomachinery blade vibration amplitude measurement through tip timing with capacitance tip clearance probes, Sensors and Actuators A: Physical 118 (1) (2005) 14–24.

[11] A. Kempe, S. Schlamp, T. Rösgen, K. Haffner, Spatial and temporal high-resolution optical tip-clearance probe for harsh environments, in: Proceedings of the 13th International Symposium on Applications of Laser Techniques to Fluid Mechanics, Lisbon, Portugal, Citeseer, 26–29, 2006.

[12] A. G. Sheard, Blade by Blade Tip Clearance Measurement, International Journal of Rotating Machinery 2011 (2011) 1–13.

[13] I. Garcia, J. Beloki, J. Zubia, G. Durana, G. Aldabaldetreku, Turbine-blade tip clearance and tip timing measurements using an optical fiber bundle sensor, in: Optical Measurement Systems for Industrial Inspection VIII, vol. 8788, International Society for Optics and Photonics, 87883H, 2013.

[14] I. García, J. Beloki, J. Zubia, G. Aldabaldetreku, M. A. Illarramendi, F. Jiménez, An optical fiber bundle sensor for tip clearance and tip timing measurements in a turbine rig, Sensors 13 (6) (2013) 7385–7398.

[15] H. Guo, F. Duan, Z. Cheng, Numerical analysis of the blade tip-timing signal of a fiber bundle sensor probe, Optical Engineering 54 (3) (2015) 034103.

[16] J. García-Martín, J. Gómez-Gil, E. Vázquez-Sánchez, Non-destructive techniques based on eddy current testing, Sensors 11 (3) (2011) 2525–2565.

[17] M. Lackner, Vibration and crack detection in gas turbine engine compressor blades using eddy current sensors, Ph.D. thesis, Massachusetts Institute of Technology, 2003.

[18] M. Rahman, R. Marklein, Advanced techniques for modelling and detection of cracks in hot wire steel, in: Proceedings on the 9th European Conference on NDT (ECNDT), Berlin, Germany, We.2.3.2, 2006.

[19] K. Chana, D. Cardwell, The use of eddy current sensor based blade tip timing for FOD detection, in: ASME Turbo Expo 2008: Power for Land, Sea, and Air, American Society of Mechanical Engineers, 169–178, 2008.

[20] D. Cardwell, K. Chana, P. Russhard, The use of eddy current sensors for the measurement of rotor blade tip timing: sensor development and engine testing, in: ASME Turbo Expo 2008: Power for Land, Sea, and Air, American Society of Mechanical Engineers, 179–189, 2008.

[21] K. Chana, D. Cardwell, L. Gray, B. Hall, Disk crack detection and prognosis using non contact time of arrival sensors, in: ASME 2011 Turbo Expo: Turbine Technical Conference and Exposition, vol. Volume 6: Structures and Dynamics, Parts A and B, American Society of Mechanical Engineers, Vancouver, British Columbia, Canada, 11–18, 2011.

[22] C. Mandache, T. Mcelhinney, N. Mrad, Aircraft engine blade tip monitoring using pulsed Eddy current technology, in: Proceedings of the 4th International Symposium on NDT in Aerospace, Augsburg, Germany, 13–15, 2012.

[23] C. Liu, D. Jiang, Improved blade tip timing in blade vibration monitoring with torsional vibration of the rotor, in: Journal of Physics: Conference Series, vol. 364, IOP Publishing, 012136, 2012.

[24] W. C. Haase, Z. S. Haase, Advances in through-the-case eddy current sensors, in: Aerospace Conference, 2013 IEEE, Big Sky, MT, USA, IEEE, 1–5, 2013.

[25] S. S. Guru, S. Shylaja, S. Kumar, R. Murthy, Pre-emptive rotor blade damage identification by blade tip timing method, Journal of Engineering for Gas Turbines and Power 136 (7) (2014) 072503.

[26] K. Karakoc, E. J. Park, A. Suleman, Improved braking torque generation capacity of an eddy current brake with time varying magnetic fields: A numerical study, Finite elements in Analysis and Design 59 (2012) 66–75.

[27] K. Karakoc, A. Suleman, E. J. Park, Analytical modeling of eddy current brakes with the application of time varying magnetic fields, Applied Mathematical Modelling 40 (2) (2016) 1168–1179.

[28] A. Rosell, G. Persson, Finite element modelling of closed cracks in eddy current testing, International Journal of fatigue 41 (2012) 30–38.

[29] J. Wu, Y. Sun, B. Feng, Y. Kang, The effect of motion-induced eddy current on circumferential magnetization in MFL testing for a steel pipe, IEEE Transactions on Magnetics 53 (7) (2017) 1–6.

[30] Z. Kubín, T. Mísek, J. Hlous, T. Dadaková, J. Kellner, T. Bachorec, Calibration of blade tip-timing sensor for shrouded 40" last stage blade, Mechanical Systems and Signal Processing 108 (2018) 88–98.

[31] R. Pohl, A. Erhard, H.-J. Montag, H.-M. Thomas, H. Wüstenberg, NDT techniques for railroad wheel and gauge corner inspection, NDT & e International 37 (2) (2004) 89–94.

[32] N. Jamia, M. I. Friswell, S. El-Borgi, R. Fernandes, Simulating eddy current sensor outputs for blade tip timing, Advances in Mechanical Engineering 10 (1) (2018) 1687814017748020.

[33] E. Weststrate, M. Steinback, N. M. Rensing, T. Tiernan, Comsol multiphysics modeling for design optimization of eddy current crack detectors, in: Proceedings of the COMSOL Conference, Boston, 2010.

[34] C. Teolis, A. Teolis, J. Paduano, M. Lackner, Analytic representation of eddy current sensor data for fault diagnostics, in: Aerospace Conference, 2005 IEEE, IEEE, 3496–3506, 2005.

[35] R. Szczepanik, R. Przysowa, J. Spychaa, E. Rokicki, K. Kazmierczak, P. Majewski, Application of Blade-Tip Sensors to Blade-Vibration Monitoring in Gas Turbines, in: Thermal Power Plants, chap. 8, InTech, 145–176, 2012.

[36] G. L. Forbes, R. B. Randall, Estimation of turbine blade natural frequencies from casing pressure and vibration measurements, Mechanical Systems and Signal Processing 36 (2) (2013) 549–561.

[37] T. M. Pickering, Methods for Validation of a Turbomachinery Rotor Blade Tip Timing System, Ph.D. thesis, Virginia Tech, 2014.

[38] A. A. Gubran, J. K. Sinha, Shaft instantaneous angular speed for blade vibration in rotating machine, Mechanical Systems and Signal Processing 44 (1-2) (2014) 47–59.